



Nitrogen-doped porous carbon nanoparticle derived from nitrogen containing conjugated microporous polymer as high performance lithium battery anode

Qingtang Zhang*, Qinqin Dai, Chao Yan, Ce Su, An Li

School of Petrochemical Engineering, Lanzhou University of Technology, Lanzhou, 730050, China

ARTICLE INFO

Article history:

Received 1 February 2017

Received in revised form

14 April 2017

Accepted 19 April 2017

Available online 22 April 2017

Keywords:

Nitrogen containing conjugated microporous polymer

Nitrogen-doped porous carbon nanoparticles

Anode

Lithium ion battery

ABSTRACT

Nitrogen-doped porous carbon nanoparticle (NPCN) was obtained by pyrolyzing nitrogen containing conjugated microporous polymer (NCMP). KOH high temperature activation following HNO_3 neutralizing was also employed to acquire NPCN-KOH with improved porous structure. NPCN and NPCN-KOH were characterized by SEM, TEM, XPS, Raman spectroscopy, BET, cyclic voltammetry and charge-discharge test. SEM results indicate that both NPCN and NPCN-KOH are nanoparticles with a size about 100 nm. TEM results imply that KOH activation promotes the catalyst granules fusing together to form large particles in NPCN-KOH. XPS and elemental analysis indicate HNO_3 neutralizing can increase the nitrogen content. Raman spectroscopy indicate NPCN-KOH possess more disordered structure. BET analysis reveals that specific surface area of NPCN-KOH is $1845 \text{ m}^2 \text{ g}^{-1}$, which is much larger than that of NPCN. These unique features ensure NPCN-KOH exhibit high reversible capacity, large rate performance and long cycling life. NPCN-KOH delivers a reversible capacity of 818 mA h g^{-1} . In addition, the capacity of NPCN-KOH cycled at 1 C for 600 cycles is as high as 527 mA h g^{-1} , with a capacity retention ratio of 97.6%.

© 2017 Elsevier B.V. All rights reserved.

1. Introduction

After dominating portable power source for cell phone, digital camera, laptop, tablet computer, and so on, lithium ion batteries (LIBs) have already emerged as the prime new energy devices for electric vehicles, hybrid electric vehicles and energy storage due to their high energy density, large rate capability, long cycle life as well as environmental benign [1–6]. These ever increasing applications of LIBs promote the urgent demand for electrode materials with both high capacity and rate capability. However, the most popular graphite anode materials suffer from a low specific capacity (theoretical capacity of graphite is 372 mA h g^{-1}) [6] and poor rate performance induced by the slow lithium ion diffusion rate. Obviously, graphite anode materials cannot meet the increasing demands of commercial LIBs market. Thus, much effort has been performed to develop other kinds of carbon materials with high energy density and large rate performance [7–12].

* Corresponding author. Address: School of Petrochemical Engineering, Lanzhou University of Technology, No. 36 Pengjiaping, Qilihe District, Lanzhou, Gansu Province 730050, China. Tel.: +86 931 7823127.

E-mail address: zhqt137@163.com (Q. Zhang).

Porous carbon is one kind of these carbon materials. It has been intensely investigated because it possesses high specific capacity, large rate performance and long cycling stability due to its porous structure, high specific area and good electronic conductivity. Nitrogen doping is matter-of-course attractive for improving the lithium storage capacity of porous carbon because of the following reason. The atomic diameter of nitrogen is smaller and the electronegativity of nitrogen (3.04) is higher than that of carbon (2.55). As a consequence, the stronger interactions between the lithium and nitrogen doped porous carbon might be very beneficial for the lithium insertion. Therefore, great deals of efforts have been performed on the nitrogen doped porous carbon with various shapes [9–19]. Besides porous carbon, nitrogen doping has been used to generate defects in carbon nanotubes or graphene and provide more active sites for lithium insertion [20,21]. In addition, nitrogen doping has been found to enhance the electronic conductivity of carbon based materials, which have been proved by several groups [22–24]. Therefore, nitrogen doping is a feasible way to improve the lithium storage performance of carbon based materials. To date, several methods have been employed to prepare nitrogen-doped carbon materials such as thermal annealing with ammonia [8], treating with HNO_3 [9] and pyrolysis of nitrogen-containing

precursors such as dopamine [10], polymer [11–15], and biomass [16–19].

Conjugated microporous polymer (CMP) combines porous structures and π -conjugated skeletons constituted by rigid aromatic rings and carbon carbon triple bonds. These specific structures make CMP possesses high chemical, thermal stability and desirable porous structure. Therefore, CMP is widely applied in various domains such as electrodes [7,25,26], catalysis [27], carbon dioxide capture [28] and volatile iodine capture [29,30], etc. More interesting, CMP is the ideal precursor to construct porous carbon because of their tuned porous structure and π -conjugated skeletons. The cross-coupling strategy via palladium-catalyzed cross-coupling or homocoupling chemistry is the typical approach to manufacture CMP. In the process of preparation, it is very possible to construct nitrogen containing CMP (NCMP) simply by choosing suitable nitrogen-containing monomer. Then, nitrogen-doped porous carbon nanoparticle (NPCN) can be logically achieved by pyrolyzing NCMP. To the best of our knowledge, NCMP derived NPCN have rarely been prepared and never been investigated as anode materials for LIBs. In this study, NPCN was prepared from NCMP, which is synthesized through palladium-catalyzed Sonogashira–Hagihara crosscoupling condensation of 1,3,5-triethynylbenzene and bis(4-bromophenyl)amine. In order to further improve its porous structure, KOH adsorbed NCMP was pyrolyzed and then neutralized with nitric acid (HNO_3) to obtain NPCN-KOH. NPCN-KOH should show a more developed porous structure. Exploring the structure and electrochemical performance of these NPCN based material is a fascinating issue for the anode materials for LIBs.

2. Experimental

2.1. Sample preparation

1,3,5-triethynylbenzene was obtained from TCI. Bis(4-bromophenyl)amine, tetrakis-(triphenylphosphine) palladium(0) and CuI were purchased from J&K Scientific. All chemicals were used without any purified. 1,3,5-triethynylbenzene and bis(4-bromophenyl)amine were used to synthesize NCMP through Pd(0)/Cu(I) catalyzed Sonogashira–Hagihara cross-coupling polycondensation (Fig. S1). 50 mg CuI, 150 mg tetrakis-(triphenylphosphine)palladium(0), 1.5 mmol 1,3,5-triethynylbenzene and 1.5 mmol bis(4-bromophenyl)amine were put into the mixture of 7.5 mL toluene and 7.5 mL triethylamine in a 50 mL two-neck round-bottom flask under N_2 protection. The mixture was stirred constantly at 100°C for 72 h. After cooling to the room temperature, the resulting NCMP was firstly filtered and washed with chloroform, acetone, water and methanol for several times to remove the unreacted monomer or catalyst residues. Then, the obtained NCMP was purified by Soxhlet extraction with methanol for 72 h. Subsequently, NCMP was dried at 70°C for 24 h.

NCMP was pre-charred at 350°C for 2 h, and then kept at 650°C for 4 h under N_2 protection to prepare NPCN. For synthesis of NPCN-KOH, 450 mg KOH was firstly dissolved in 10 mL ethanol. Then, 150 mg NCMP was put into the solution and stirred constantly to get the NCMP-KOH mixture. Secondly, the mixture was also pre-charred at 350°C for 2 h, and then kept at 650°C for 4 h under the N_2 protection. Then, the resulting mixture was neutralized with dilute HNO_3 and then washed with deionized water for several times to obtain NPCN-KOH.

2.2. Characterization

CR2032 coin-type cells were assembled to evaluate the electrochemical properties of NPCN and NPCN-KOH. The electrode was

prepared by spreading a mixture of 80% NPCN or NPCN-KOH, 10% super P, and 10% LA132 aqueous binder onto a copper foil. Then, it was dried at 100°C for 8 h in vacuum. The active material loading of all the electrodes is about 1.26 mg cm^{-2} . The cells are composed of the electrode, and lithium flake counter electrode separated by a microporous polypropylene separator (Celgard 2400). The electrolyte is 1 mol L^{-1} LiPF_6 in a mixture of ethylene carbonate/dimethyl carbonate/ethyl-methyl carbonate (EC/DMC/EMC). The volume of electrolyte used in every CR2032 cell is about 0.05 mL. The cells were discharge/charged in the voltage range of 0.0–3.0 V on a LAND CT2001A battery tester. The current density of 1 C is 550 mA h g^{-1} . The cyclic voltammetry (CV) analysis of the fresh cells were performed on an electrochemical workstation (ZF100, Shanghai Zhengfang Electronics Co., Ltd). Electrochemical impedance spectra (EIS) of the fresh cells were investigated using an electrochemical workstation (CHI660E, Shanghai Chenhua Instruments Co., China).

The morphologies of NPCN and NPCN-KOH were examined by scanning electron microscopy (SEM) and high resolution transmission electron microscopy (TEM) (JEOL JSM 2100F). Energy-dispersive X-ray spectroscopy (EDX) was used to determine the elemental composition of NPCN and NPCN-KOH. The porous properties of NPCN and NPCN-KOH were evaluated by nitrogen adsorption/desorption analysis at -196°C using a micromeritics ASAP 2020 apparatus. Raman spectra was recorded on a Horiba JY HR800 confocal microscope Raman spectrometer. X-ray photoelectron spectroscopy (XPS) measurements were performed on an ESCALAB 250Xi. An elemental analysis instrument (Elementar Analysensysteme GmbH) was used to determine the elemental composition of NPCN and NPCN-KOH.

3. Results and discussion

Fig. 1 presents the SEM images of NPCN and NPCN-KOH. The micro morphologies of both samples seem very similar. As shown in Fig. 1c and f, they are both aggregates composed of nanoparticles with a size about 100 nm. This indicates that KOH high temperature activation following HNO_3 neutralizing can not destroy the morphology of NPCN. The micro morphologies of NPCN and NPCN-KOH are also very similar to that of their precursor NCMP (Fig. S1, Supporting information). NCMP is also the aggregates composed of primary nanoparticles with a size of 100 nm. These imply that CMP can well keep their morphology during the rigorous pyrolysis procedure, which has been proved in our previous work [7,26]. It gives a chance to tune the morphology of NPCN simply by tuning the morphology of CMP.

Fig. 2 is the TEM images of NPCN and NPCN-KOH. It is difficult to ascertain the sizes of primary nanoparticles in both TEM images, because both NPCN and NPCN-KOH are the aggregates with primary nanoparticles. As shown in Fig. 2a, many small nanoparticles with a size of 20 nm are observed in the NPCN sample. The EDX spot scan at red rectangle area (Fig. 2a) is depicted as Fig. 2c, which reveals that Pd and O elementals are detected despite of the main composition carbon. The strong peak of Cu is attributed to the copper mesh substrate for TEM. Therefore, these small nanoparticles should be the residual catalyst granules. Differently, there are few large nanoparticles with a size of 100 nm in Fig. 2b. Fig. 2d is the EDX spot scan of one of these nanoparticles (red rectangle area Fig. 2b), which reveals that the elemental compositions of the large nanoparticles are just similar to those small nanoparticles of NPCN. These results indicate that KOH high temperature activation may etch carbon interface between the small catalyst granules and then the small catalyst granules are fused into large nanoparticles. XRD analysis discloses that strong crystal peaks are observed in NPCN-KOH (Fig. S3, Supporting information), also suggesting that large

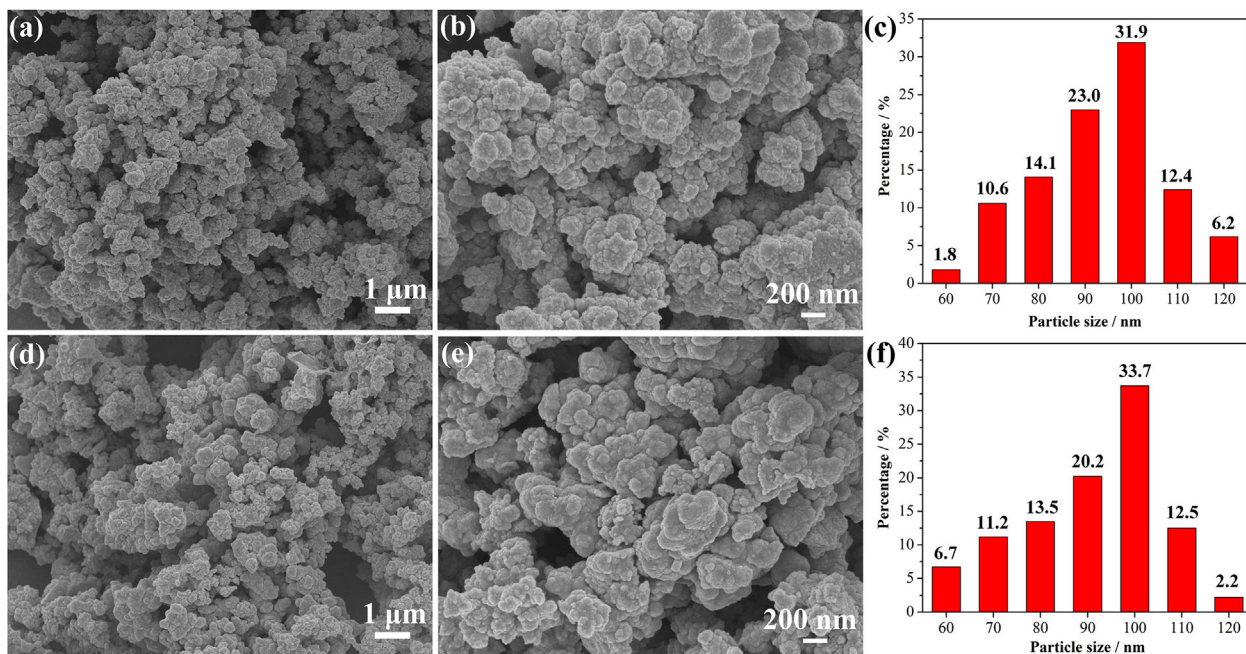


Fig. 1. SEM images of NPCN (a, b) and NPCN-KOH (d, e). Particle size distributions of NPCN (c) and NPCN-KOH (f) analyzed from SEM images.

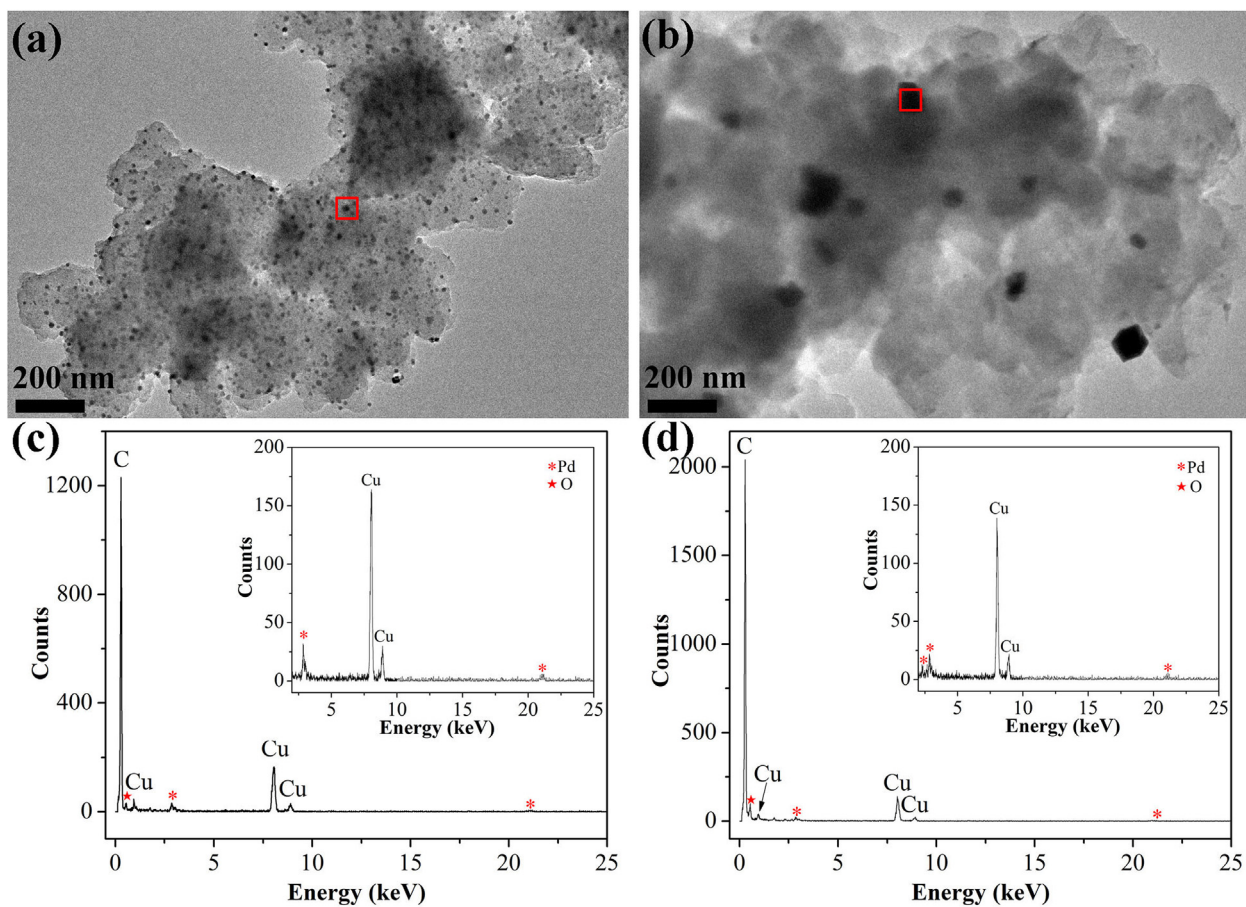


Fig. 2. TEM images (a,b) and EDX spot scan (c,d) of NPCN and NPCN-KOH.

size catalyst granules are formed in NPCN-KOH.

As shown in Fig. 3, elemental mapping of the orange rectangle

area is investigated by EDX to confirm the N distribution in NPCN-KOH. Fig. 3b reveals that the shape of carbon elemental mapping

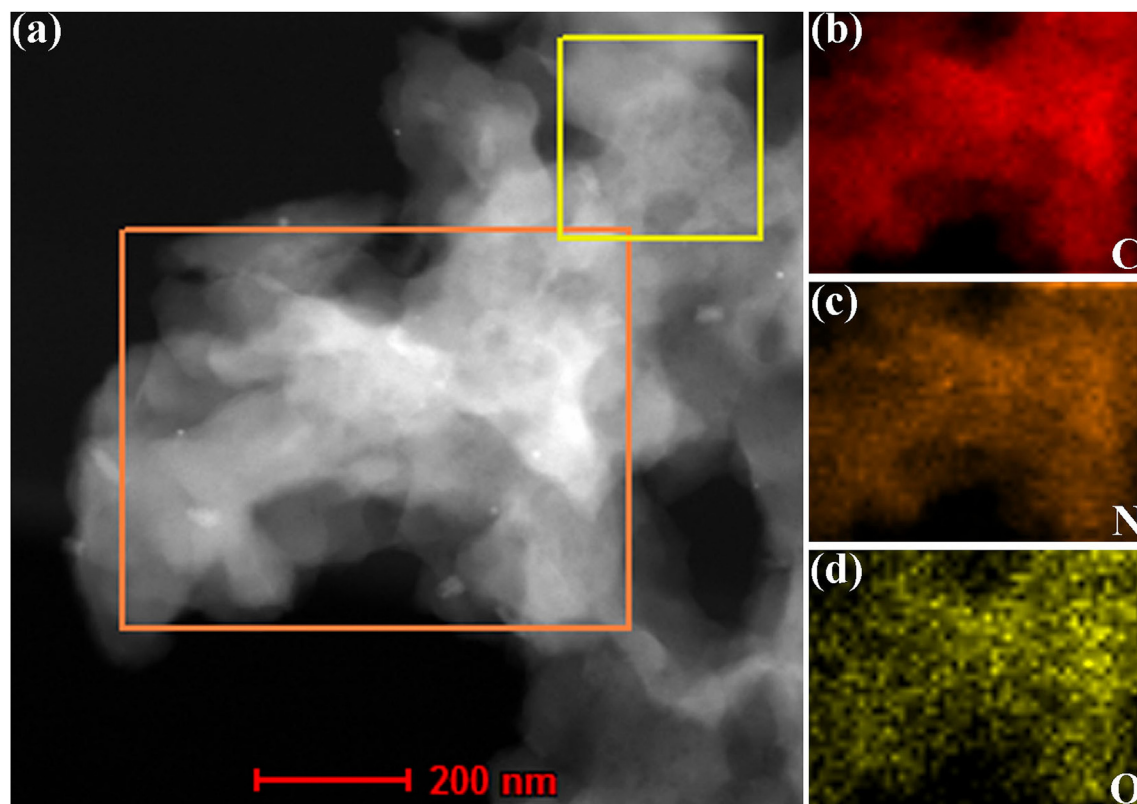


Fig. 3. TEM-EDX mapping of NPCN-KOH.

(red) is very similar to the morphology of the choosing area of NPCN-KOH (Fig. 3a). Fig. 3c further indicates that N element is homogeneously distributed with C element. Fig. 3d reveals that O element is also homogeneously distributed with C element. In addition, N and O element are dispersed uniformly with C element in the NPCN (Fig. S3, Supporting information). Elemental mapping of NPCN also intuitively proved that separated Pd nanoparticles are dispersed in NPCN.

The chemical composition and nature of nitrogen (N) species of NPCN as well as NPCN-KOH were determined by XPS. The survey XPS spectrum (Fig. 4) clearly indicates C1s, O1s and N1s peaks appeared in both samples. In addition, weak Pd3d peak is also observed in both samples. Pd impurity is decomposition product of the residual catalyst to synthesize NCMP. The atomic percentage of Pd in the carbon material is about 0.27% based on XPS result. As shown in Fig. 4b, the high-resolution C1s peak can be deconvoluted into three components located around 284.7, 285.3 and 288.2 eV. The main peak at 284.7 eV is assigned to be typical sp^2 graphitic carbon. The weak peaks at 285.3 eV and 288.2 eV imply the N atoms bonding to be sp^2 -C and sp^3 -C atoms, respectively [13]. The high resolution N1s spectra of NPCN and NPCN-KOH are shown as Fig. 4d. The deconvoluted peaks at 398.6, 400.3, 401.1 and 405.1 eV can be assigned to be pyridine N, pyrrole N, graphite N and nitro N, respectively [31]. The peak intensity of NPCN-KOH is obviously stronger than that of NPCN, implying the higher N content of NPCN-KOH. The atomic percentages of doped N for NPCN and NPCN-KOH were calculated to be 0.62% and 2.87%, respectively. It reveals that HNO_3 neutralizing can obviously increase N content of samples. Raman spectroscopy is further employed to detect the subtle structural variation in NPCN and NPCN-KOH. Raman spectra of both samples are shown as Fig. 4d. Strong D bands centered at 1353 cm^{-1} and G band centered at 1585 cm^{-1} are observed for both

samples. D bands are related to the edges, other defects and disordered carbon, while G bands are corresponded to the ordered sp^2 hybrid carbon [11–14]. Generally, the disorder degree of carbon material is estimated by the intensity ratio of D band to G band (I_D/I_G). The I_D/I_G of NPCN is 0.86, while that of NPCN-KOH is 0.96. This implies that NPCN-KOH possesses more disordered structures or defects. It is consistent with the XPS results that more N doping generates more defects.

N contents of NPCN and NPCN-KOH are also determined by elemental analysis. The N contents of NPCN and NPCN-KOH are 0.80 wt% and 2.05 wt%, which are slightly different from the XPS results (N contents of XPS results are atomic percentages). The elemental analysis confirms that the N content of NCMP is 0.71% (Supporting information), which is even lower than that of NPCN. It reveals that N content suffers nearly zero loss during the pyrolysis to obtain NPCN and N element is stable in π -conjugated skeletons at high temperature. It implies that the N content can be controlled simply by controlling the N content of NCMP.

The pore properties of NPCN and NPCN-KOH were investigated using isothermal N_2 adsorption-desorption at $-196\text{ }^\circ\text{C}$ using a micromeritics ASAP 2020 apparatus. Seen from Fig. 5a, both isotherms are type IV isotherm curves, exhibiting a typical H1 hysteresis loop at moderate relative pressures (between 0.4 and 0.5 P/P_0). It implies that NPCN and NPCN-KOH both possess a lot of mesopores [10]. Estimated from the amount of nitrogen adsorbed at a relative pressure of $P/P_0 = 0.99$, the pore volumes of NPCN and NPCN-KOH were 0.34 and $0.96\text{ cm}^3\text{ g}^{-1}$, respectively. It reveals that KOH high temperature activation can greatly increase the pore volume. The Brunauer-Emmett-Teller (BET) surface areas for NPCN and NPCN-KOH are 634 and $1845\text{ m}^2\text{ g}^{-1}$, respectively. The later is nearly three times as large as the former. The large surface area is very beneficial for the electrolyte access [9]. The pore size

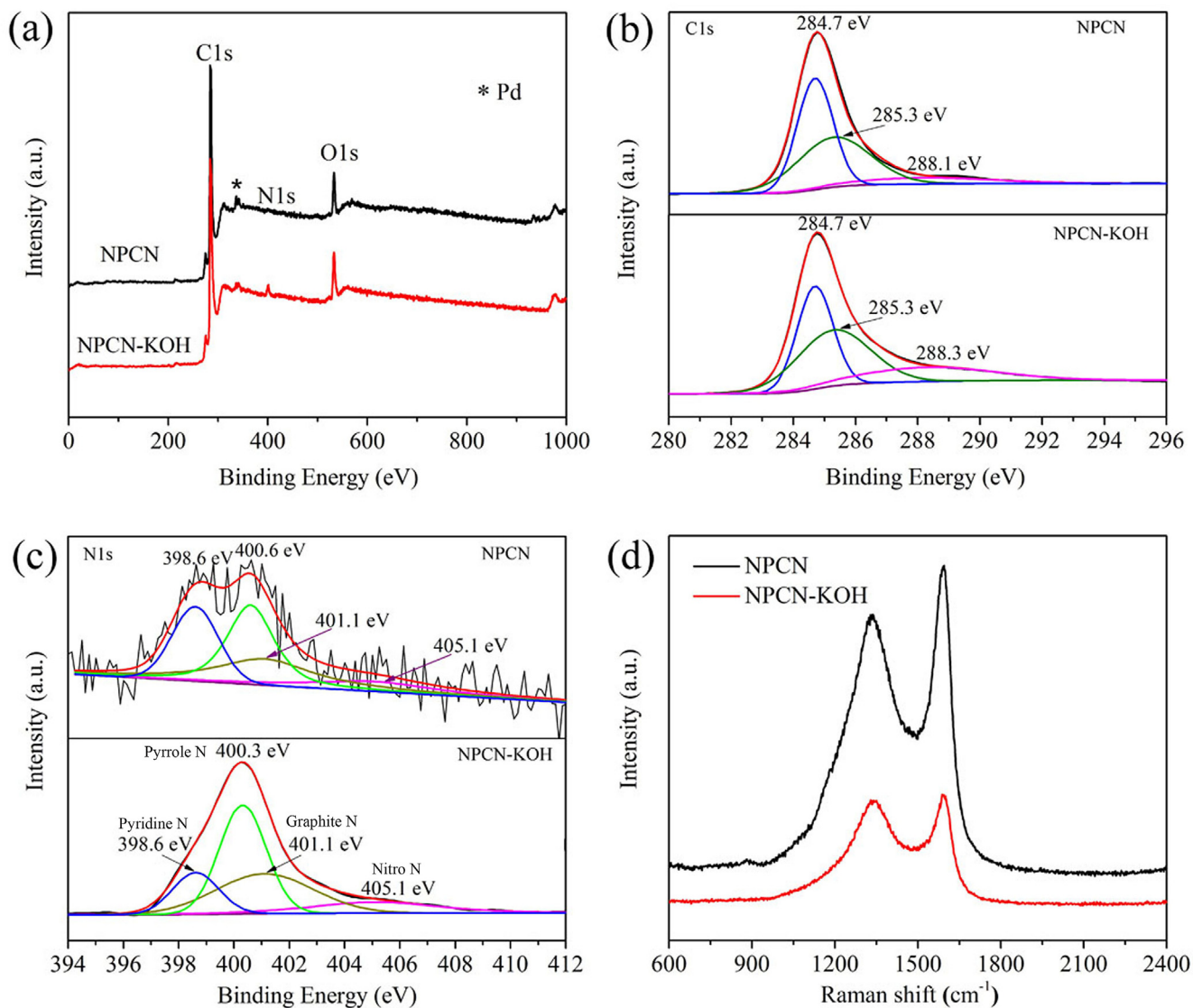


Fig. 4. XPS spectra for NPCN and NPCN-KOH (Survey scan a, high resolution of C1s b and high resolution of N1s c). Raman spectrum for NPCN and NPCN-KOH (d).

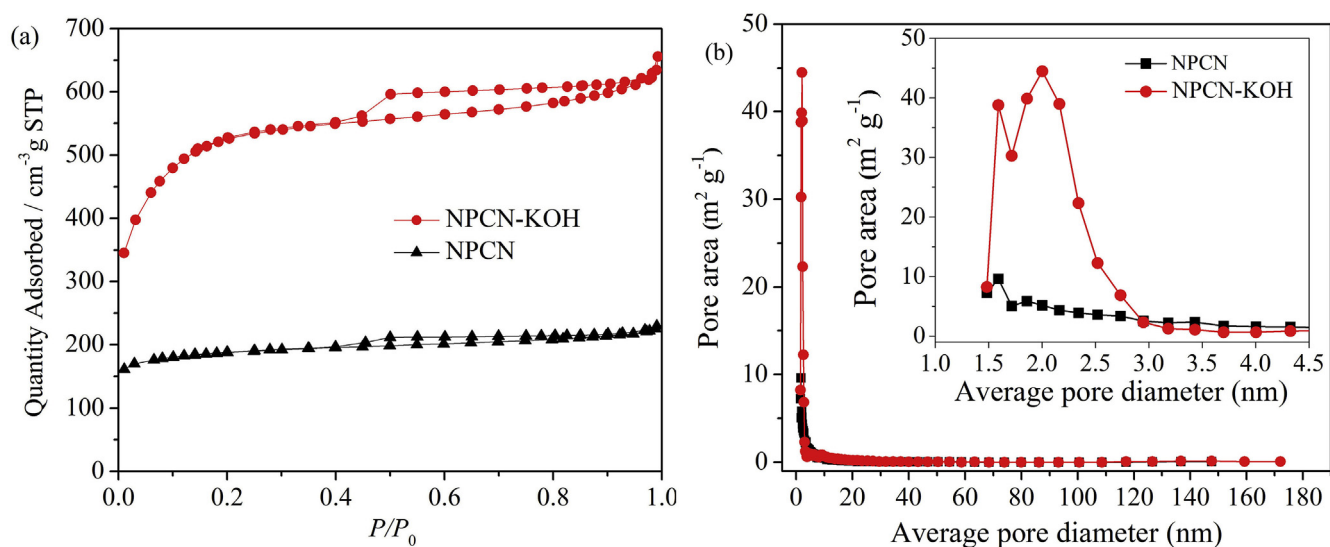


Fig. 5. (a) Nitrogen adsorption-desorption isotherms of NPCN and NPCN-KOH. (b) Pore size distribution of NPCN and NPCN-KOH.

distribution is analyzed by the nonlocal density functional theory (NLDFT) method (Fig. 5b). The largest pore size of NPCN-KOH is 172 nm, which is distinctly higher than that of NPCN (148 nm). So, NPCN-KOH has a broader pore size distribution compared to NPCN, attributing to that some macropores of NPCN are enlarged by KOH etching. The external pore (larger than 2 nm) areas of NPCN-KOH and NPCN are measured to be 828 and 154 m² g⁻¹, respectively. Generally, KOH activation is used to increase the microporous surface area. But, here KOH activation obviously enhances the meso/macro porous surface area of NPCN. The reason may be as the following. TEM have disclosed that KOH activation etch carbon interface between the small catalyst granules and then the small catalyst granules are fused into large nanoparticles. As a result, more mesopores and macropores are generated in the process to prepare NPCN-KOH. As shown in Fig. 5b inset, the micropore area of NPCN-KOH is clearly increased. The micropore (less than 2 nm) areas of NPCN-KOH and NPCN are measured to be 1017 and 480 m² g⁻¹, respectively. The pore volume and BET surface area for NCMP is measured to be 0.26 cm³ g⁻¹ and 418 m² g⁻¹ (Fig. S4b, Supporting information). The values are lower than those of NPCN, indicating more pores are generated during the pyrolysis of NCMP.

CR2032 coin-type cells were assembled to evaluate the electrochemical behaviors of the NPCN and NPCN-KOH. The active material loadings of all the electrodes are controlled to be about

1.26 mg cm⁻². CV profiles were recorded with a scan rate of 0.1 mV s⁻¹. The voltage window of CV analysis is in the range of 0.0–3.0 V. CV profiles were depicted for the first (Fig. 6a) and third (Fig. 6b) cycles. NPCN and NPCN-KOH show typical CV curves of the carbonaceous anode materials [8,9,26]. For the first CV scan in Fig. 6a, both samples show a broad cathodic peak at 0.2–0.9 V, which disappears in the subsequent cycles, indicating some irreversible reactions and the formation of a solid electrolyte interface (SEI) layer [10,26]. The sharp peaks around 0 V, assigned to Li⁺ insertion into the carbonaceous materials, are observed for NPCN and NPCN-KOH. The anodic peak at 2.36 V can be assigned to the formation of CuO [32,33]. But, the CuI (catalyst) has been removed from the carbon particles. Elemental mapping has also proved that there is no Cu in the carbon particles (Fig. 3). Therefore, such copper oxides may be formed during storage of the commercial copper foil, which is used as current collector for anodes [16]. NPCN-KOH displays a different CV profile from NPCN, suggesting other lithium storage reactions exist in NPCN-KOH. The rectangular shape of the CV profiles at high potentials in anodic scan suggests that the capacitive lithium storage behaviors are actually existed in the NPCN-KOH [16]. It may be attributed to the much higher BET surface area of NPCN-KOH. Moreover, CV plots of NPCN-KOH cover a much large area than that of NPCN in the third CV scan (Fig. 6b), implying a much higher specific capacity of NPCN-KOH.

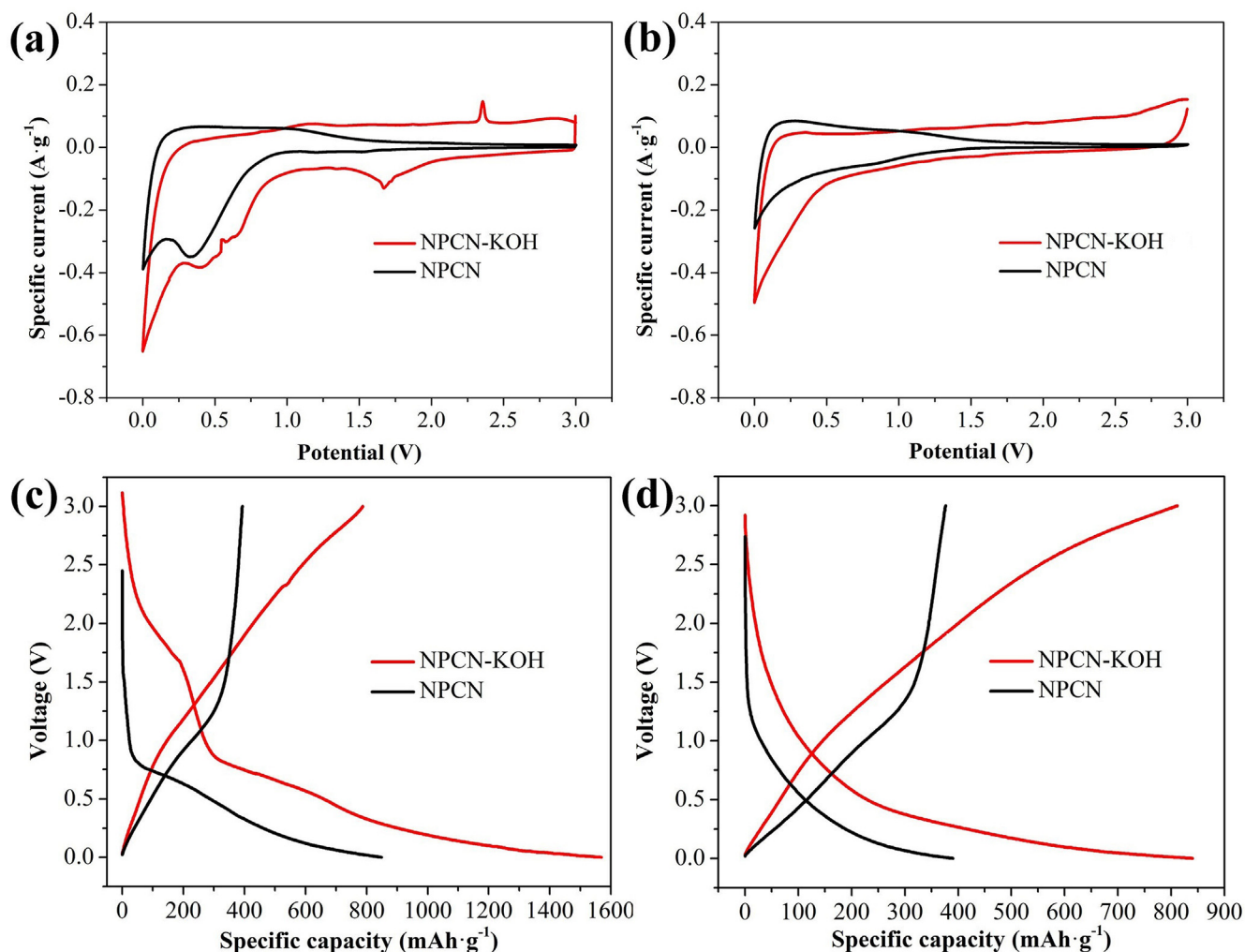


Fig. 6. CV curves of at a scan rate of 0.1 mV s⁻¹ (a) first cycle and (b) third cycle. Discharge–charge voltage curves (c) first cycle and (d) fifth cycle.

With the voltage ranging from 0.0 to 3.0 V, the discharge-charge (lithiation-delithiation) curves at a current rate of 0.2 C are presented in Fig. 6c and d. During the first discharge (lithiation) process (Fig. 6c), an obvious long voltage plateau around 0.6 V is found for NPCN and NPCN-KOH. It can be ascribed to the SEI layer formation and some irreversible reactions, resulting in the large irreversible capacity in the first cycle [8]. Observed from Fig. 6c, the initial discharge and charge (delithiation) capacities for NPCN-KOH are 1570 and 788 mA h g⁻¹, while those for NPCN are 849 and 393 mA h g⁻¹. So, the initial coulombic efficiencies of NPCN-KOH and NPCN are 50.2% and 46.3%. Tremendous BET surface area is increased through KOH activation following HNO₃ neutralizing. As a result, the increased pores are beneficial for lithium storage capacity. So, NPCN-KOH possesses much higher specific capacity. Fig. 6d is the fifth discharge-charge curve. It reveals that the specific capacities of NPCN-KOH are much higher than those of NPCN. The fifth discharge and charge capacities of NPCN-KOH are 840 and 812 mA h g⁻¹. So, the NPCN-KOH has a fifth coulombic efficiency of 96.7%. Similarly, the discharge capacity, charge capacity and fifth coulombic efficiency are found to be 390 mA h g⁻¹, 377 mA h g⁻¹ and 96.7%. Therefore, coulombic efficiencies of NPCN-KOH and NPCN have been greatly increased at the fifth cycles.

NPCN and NPCN-KOH were discharged-charged at increasing current rates from 0.2 to 30 C each for five cycles to roundly estimate the rate performance. As shown in Fig. 7, the NPCN-KOH exhibits obviously higher capacity over NPCN at every current rate. The reversible capacities (third charge capacity at every rate) of NPCN-KOH are 818, 660, 490, 408, 311, 291, 241, 207, 166 and 159 mA h g⁻¹ at the current rate of 0.1, 0.2, 0.5, 1, 2, 3, 5, 10, 20 and 30 C. While restored at 0.1 C, the reversible capacity of NPCN-KOH is 857 mA h g⁻¹. This value is higher than other porous carbon [7–9,14]. NPCN delivers reversible capacities of 416, 346, 267, 232, 195, 185, 166, 138, 122 and 114 mA h g⁻¹, respectively. While restored at 0.1 C, the reversible capacity of NPCN is only 366 mA h g⁻¹. This value is much lower than that of NPCN-KOH (857 mA h g⁻¹). Obviously, the rate performance of NPCN-KOH is much higher than that of NPCN. The superior rate performance of NPCN-KOH may be due to its porous structure and doped nitrogen content. The external pore (larger than 2 nm) area for NPCN-KOH is 828 m² g⁻¹. While that for NPCN is only 154 m² g⁻¹. The numerous external pores can act as reservoirs for electrolyte, facilitating the rapid charge-transfer reactions [5,8]. In addition, the amounts of

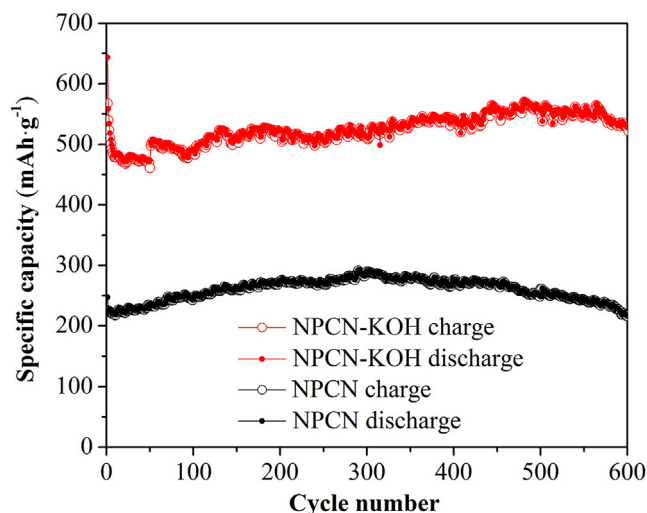


Fig. 8. Comparisons of the cycling performance of NPCN and NPCN-KOH at a charge-discharge rate of 1 C for 600 cycles.

nanopores in sample can be very effective in lithium storage. Meanwhile, nitrogen-doping offers more active sites for lithium insertion. The N content of NPCN-KOH is much higher than that of NPCN, having been proved by XPS and elemental analysis.

The cycling performance of NPCN and NPCN-KOH was measured at a 1 C for 600 cycles after three discharge-charge activations at 0.2 C. The results were compared and depicted as Fig. 8. Seen from Fig. 8, the second and 600th reversible capacities of NPCN-KOH are 540 and 527 mA h g⁻¹, while, the second and 600th reversible capacities of NPCN are 225 and 216 mA h g⁻¹, respectively. Therefore, the capacity retention ratios of NPCN-KOH and NPCN are calculated to be 97.6% and 96.0%, respectively. NPCN-KOH and NPCN both exhibit good cycling performance. The much high BET surface area and high N content of NPCN-KOH provide much more active sites for lithium storage, which should be responsible for the high specific capacity at 1 C. The coulombic efficiencies of NPCN-KOH and NPCN are very similar. Most of the coulombic efficiencies are about 99% (Fig. S5, Supporting information).

EIS is a powerful technique to provide plenty of information

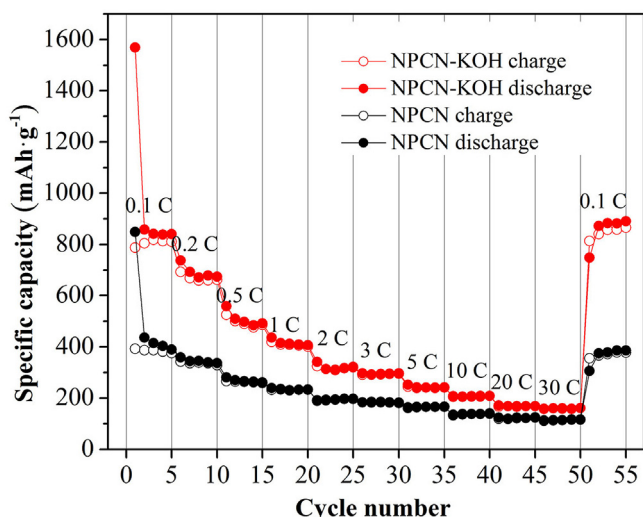


Fig. 7. Rate performance of NPCN and NPCN-KOH.

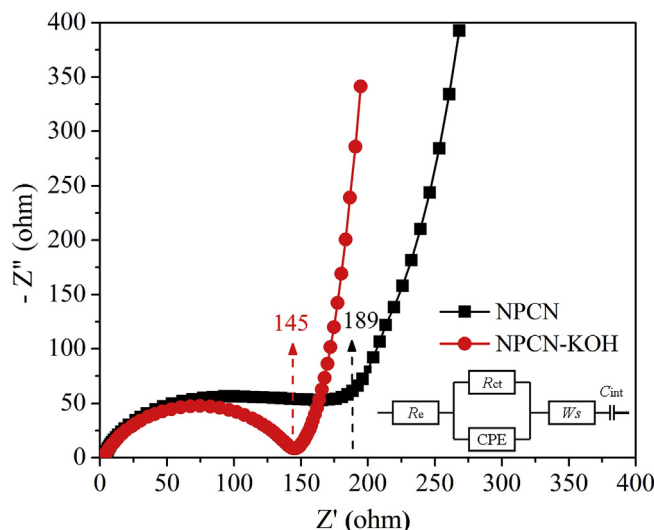


Fig. 9. EIS of the fresh cells loaded with NPCN and NPCN-KOH.

with respect to the lithium diffusion impedance and the interfacial charge transfer resistance between the electrode and electrolyte. So, EIS was employed to investigate the fundamental reason for the different electrochemical performance of the two samples. The fresh cells are chosen to investigate the EIS of NPCN and NPCN-KOH at room temperature. As shown in Fig. 9, both samples show same Nyquist plot shapes, composed of one semicircle at high frequency and a straight line at low frequency. The impedance data were fitted by an equivalent electrical circuit (Fig. 9 inset), which consists of electrolyte resistance (R_e), charge transfer resistances (R_{ct}), constant phase element (CPE), Warburg impedance (W_s) and the intercalation capacitance (C_{int}) [26]. Generally speaking, the semicircle and straight line represent the interfacial charge transfer impedance and the lithium diffusion impedance, respectively. R_e of NPCN-KOH and NPCN are 3.65 and 4.05 Ω , respectively. The low R_e of NPCN-KOH may be attributed to its more developed porous structure (the surface area of NPCN-KOH is as high as 1845 $m^2 g^{-1}$), which retain more electrolyte and allow the lithium ion permeating quickly in the electrode. Observed from Fig. 9, the charge transfer resistance of NPCN-KOH is 145 Ω and that of NPCN is 189 Ω . The line slope in low frequency of NPCN-KOH is distinctly higher than that of NPCN, indicating better lithium ion diffusion in NPCN-KOH.

4. Conclusions

NPCN was obtained simply by pyrolyzing NCMP. KOH high temperature activation following HNO_3 neutralizing was also employed to acquire NPCN-KOH with improved porous structure. SEM reveals that NPCN-KOH commendably retains the nanoparticle morphology of NPCN during the high temperature activation. However, nitrogen adsorption/desorption analysis proved that NPCN-KOH has extremely high BET surface area of 1845 $m^2 g^{-1}$, which is nearly three times as large as that of NPCN. In addition, NPCN-KOH shows a much higher external pore (larger than 2 nm) surface area. EDX and elemental analysis both proved NPCN-KOH possesses a much higher N content, which might be attributing the HNO_3 neutralizing. These distinctive structures and characters ensure NPCN-KOH exhibit better electrochemical performance. The reversible capacity of NPCN-KOH reaches up to 818 $mA h g^{-1}$ at a current rate of 0.1 C. In addition, NPCN-KOH shows much better rate performance and cycling stability (527 $mA h g^{-1}$ after 600 cycles at 1 C with a capacity retention ratio of 97.6%) over NPCN. This work brings new perspectives in preparing new kind of porous carbon with developed pores as high performance anodes for LIBs.

Acknowledgements

This research was supported by the National Nature Science Foundation of China (No. 21466020), the Gansu Provincial Science Fund (1606RJZA180) and the Foundation for Innovation Groups of Basic Research in Gansu Province (No. 1606RJA322).

Appendix A. Supplementary data

Supplementary data related to this article can be found at <http://dx.doi.org/10.1016/j.jallcom.2017.04.207>.

References

- [1] R. Marom, S.F. Amalraj, N. Leifer, D. Jacob, D. Aurbach, A review of advanced and practical lithium battery materials, *J. Mater. Chem.* 21 (2011) 9938–9954.
- [2] B. Scrosati, J. Hassoun, Y.K. Sun, Lithium-ion batteries. A look into the future, *Energy Environ. Sci.* 4 (2011) 3287–3295.
- [3] Q. Zhang, J. Mei, X. Wang, J. Guo, F. Tang, W. Lu, Facile synthesis of spherical spinel $LiMn_2O_4$ nanoparticles via solution combustion synthesis by controlling calcinating temperature, *J. Alloys Compd.* 617 (2014) 326–331.
- [4] D. Larcher, J.M. Tarascon, Towards greener and more sustainable batteries for electrical energy storage, *Nat. Chem.* 7 (2015) 19–29.
- [5] Q. Zhang, W. Fan, G. Wang, M. Qu, Z. Yu, Role of mesopores on the electrochemical performance of $LiCoO_2$ composite cathodes for lithium ion batteries, *Ionics* 17 (2011) 697–703.
- [6] G. Wang, B. Zhang, M. Yue, X. Xu, M. Qu, Z. Yu, A modified graphite anode with high initial efficiency and excellent cycle life expectation, *Solid State Ionics* 176 (2005) 905–909.
- [7] Q. Zhang, H. Sun, X. Wang, Z. Zhu, W. Liang, A. Li, S. Wen, W. Deng, Conjugated microporous polymer-derived porous hard carbon as high-rate long-life anode materials for lithium ion batteries, *Energy Technol.* 1 (2013) 721–725.
- [8] T. Chen, L. Pan, T.A. Loh, D.H. Chua, Y. Yao, Q. Chen, D. Li, W. Qin, Z. Sun, Porous nitrogen-doped carbon microspheres as anode materials for lithium ion batteries, *Dalton Trans.* 43 (2014) 14931–14935.
- [9] X. Li, X.B. Zhu, Y. Zhu, Z. Yuan, L.L. Si, Y. Qian, Porous nitrogen-doped carbon vegetable-sponges with enhanced lithium storage performance, *Carbon* 69 (2014) 515–524.
- [10] K. Huo, W. An, J. Fu, B. Gao, L. Wang, X. Peng, G.J. Cheng, P.K. Chu, Mesoporous nitrogen-doped carbon hollow spheres as high performance anodes for lithium-ion batteries, *J. Power Sources* 324 (2016) 233–238.
- [11] L. Zhang, G. Xia, Z. Guo, D. Sun, X. Li, X. Yu, In situ fabrication of three-dimensional nitrogen and boron co-doped porous carbon nanofibers for high performance lithium-ion batteries, *J. Power Sources* 324 (2016) 294–301.
- [12] X. Zhou, J. Tang, J. Yang, J. Xie, B. Huang, Seaweed-like porous carbon from the decomposition of polypyrrole nanowires for application in lithium ion batteries, *J. Mater. Chem. A* 1 (2013) 5037–5044.
- [13] H.G. Wang, Y. Wang, Y. Li, Y. Wan, Q. Duan, Exceptional electrochemical performance of nitrogen-doped porous carbon for lithium storage, *Carbon* 82 (2015) 116–123.
- [14] X. Han, P. Han, J. Yao, S. Zhang, X. Cao, J. Xiong, J. Zhang, G. Cui, Nitrogen-doped carbonized polyimide microsphere as a novel anode material for high performance lithium ion capacitors, *Electrochim. Acta* 196 (2016) 603–610.
- [15] X. Liu, J. Zhang, S. Guo, N. Pinna, Graphene/N-doped carbon sandwiched nanosheets with ultrahigh nitrogen doping for boosting lithium-ion batteries, *J. Mater. Chem. A* 4 (2016) 1423–1431.
- [16] Y. Mao, H. Duan, B. Xu, L. Zhang, Y. Hu, C. Zhao, Z. Wang, L. Chen, Y. Yang, Lithium storage in nitrogen-rich mesoporous carbon materials, *Energy Environ. Sci.* 5 (2012) 7950–7955.
- [17] V. Selvamani, R. Ravikumar, V. Suryanarayanan, D. Velayutham, S. Gopukumar, Fish scale derived nitrogen doped hierarchical porous carbon—a high rate performing anode for lithium ion cell, *Electrochim. Acta* 182 (2015) 1–10.
- [18] J. Qu, S. Lv, X. Peng, S. Tian, J. Wang, F. Gao, Nitrogen-doped porous “green carbon” derived from shrimp shell: combined effects of pore sizes and nitrogen doping on the performance of lithium sulfur battery, *J. Alloy. Compd.* 671 (2016) 17–23.
- [19] W. Lei, L. Han, C. Xuan, R. Lin, H. Liu, H.L. Xin, D. Wang, Nitrogen-doped carbon nanofibers derived from polypyrrole coated bacterial cellulose as high-performance electrode materials for supercapacitors and Li-ion batteries, *Electrochim. Acta* 210 (2016) 130–137.
- [20] L.G. Bulusheva, A.V. Okotrub, A.G. Kurennya, H. Zhang, H. Zhang, X. Chen, H. Song, Electrochemical properties of nitrogen-doped carbon nanotube anode in Li-ion batteries, *Carbon* 49 (2011) 4013–4023.
- [21] X. Li, J. Liu, Y. Zhang, Y. Li, H. Liu, X. Meng, J. Yang, D. Geng, D. Wang, R. Li, High concentration nitrogen doped carbon nanotube anodes with superior Li^+ storage performance for lithium rechargeable battery application, *J. Power Sources* 197 (2012) 238–245.
- [22] H.J. Burch, J.A. Davies, E. Brown, L. Hao, S.A. Contera, N. Grobert, J.F. Ryan, Electrical conductance and breakdown in individual CN_x multiwalled nanotubes, *Appl. Phys. Lett.* 89 (2006) 143110–143113.
- [23] J.P. Paraknowitsch, J. Zhang, D. Su, A. Thomas, M. Antonietti, Ionic liquids as precursors for nitrogen-doped graphitic carbon, *Adv. Mater.* 22 (2010) 87–92.
- [24] A. Schneider, C. Suchomski, H. Sommer, J. Janek, T. Brezesinski, Free-standing and binder-free highly N-doped carbon/sulfur cathodes with tailorable loading for high-areal-capacity lithium–sulfur batteries, *J. Mater. Chem. A* 3 (2015) 20482–20486.
- [25] S. Zhang, W. Huang, P. Hu, C. Huang, C. Shang, C. Zhang, R. Yang, G. Cui, Conjugated microporous polymers with excellent electrochemical performance for lithium and sodium storage, *J. Mater. Chem. A* 3 (2015) 1896–1901.
- [26] Q. Zhang, Q. Dai, M. Li, X. Wang, A. Li, Incorporation of MnO nanoparticles inside porous carbon nanotubes originated from conjugated microporous polymers for lithium storage, *J. Mater. Chem. A* 4 (2016) 19132–19139.
- [27] B.C. Ma, S. Ghasimi, K. Landfester, F. Vilela, A.I.Z. Kai, Conjugated microporous polymer nanoparticles with enhanced dispersibility and water compatibility for photocatalytic applications, *J. Mater. Chem. A* 3 (2015) 16064–16071.
- [28] Y. Chen, H. Sun, R. Yang, T. Wang, C. Pei, Z. Xiang, Z. Zhu, W. Liang, A. Li, W. Deng, Synthesis of conjugated microporous polymer nanotubes with large surface areas as absorbents for iodine and CO_2 uptake, *J. Mater. Chem. A* 3 (2015) 87–91.
- [29] X. Qian, Z.Q. Zhu, H.X. Sun, F. Ren, P. Mu, W. Liang, L. Chen, A. Li, Capture and reversible storage of volatile iodine by novel conjugated microporous polymers containing thiophene units, *ACS Appl. Mater. Interfaces* 8 (2016) 21063–21069.
- [30] F. Ren, Z. Zhu, X. Qian, W. Liang, P. Mu, H. Sun, J. Liu, A. Li, Novel thiophene-

- beared conjugated microporous polymer honeycomb-like porous spheres with ultrahigh iodine uptake, *Chem. Commun.* 52 (2016) 9797–9800.
- [31] C. Reitz, B. Breitung, A. Schneider, D. Wang, M. Lehr, T. Leichtweiß, J. Janek, H. Hahn, T. Brezesinski, Hierarchical carbon with high nitrogen doping level: a versatile anode and cathode host material for long-life lithium-ion and lithium-sulfur batteries, *ACS Appl. Mater. Interfaces* 8 (2016) 10274–10282.
- [32] X. Duan, H. Huang, S. Xiao, J. Deng, G. Zhou, Q. Li, T. Wang, 3D hierarchical CuO mesocrystals from ionic liquid precursors: towards better electrochemical performance for Li-ion batteries, *J. Mater. Chem. A* 4 (2016) 8402–8411.
- [33] S. Mohapatra, S.V. Nair, D. Santhanagopalan, A.K. Rai, Nanoplate and mulberry-like porous shape of CuO as anode materials for secondary lithium ion battery, *Electrochim. Acta* 206 (2016) 217–225.